Numerical simulation of blow-up solutions of the vector nonlinear Schrödinger equation

James Coleman* and Catherine Sulem†
Department of Mathematics, University of Toronto, Toronto, Canada M5S 3G3
(Received 26 February 2002; revised manuscript received 16 May 2002; published 3 September 2002)

We present numerical simulations of blow-up solutions of the vector nonlinear Schrödinger equation, which arises as the subsonic limit of the vectorial Zakharov system in plasma physics. In the course of our calculations, we observed the phenomenon of splitting of the solution profile. To capture the structure of the solution, we developed a new dynamic mesh refinement method based on the iterative grid distribution method introduced by Ren and Wang [J. Comput. Phys. **159**, 246 (2000)]. We also applied this method to study the time dispersion nonlinear Schrödinger equation that describes the propagation of ultrashort pulses in a dispersive medium.

DOI: 10.1103/PhysRevE.66.036701 PACS number(s): 02.70.Bf, 05.10.−a, 52.38.Hb

I. INTRODUCTION

The Zakharov system

$$i\partial_t \mathbf{E} - \alpha \boldsymbol{\nabla}\times(\boldsymbol{\nabla}\times\mathbf{E}) + \boldsymbol{\nabla}(\boldsymbol{\nabla}\cdot\mathbf{E}) = n\mathbf{E},$$

$$\partial_{tt} n - \Delta n = \Delta|\mathbf{E}|^2 \tag{1}$$

governs the coupled dynamics of the complex envelope of the electric-field oscillations and the low-frequency fluctuations of the ions [1] in a quasineutral plasma. In the ''subsonic limit,'' where the density fluctuations are assumed to follow adiabatically the modulation of the amplitude, the Zakharov system reduces to the vector nonlinear Schrödinger (VNLS) equation

$$i\partial_t \mathbf{E} - \alpha \boldsymbol{\nabla}\times(\boldsymbol{\nabla}\times\mathbf{E}) + \boldsymbol{\nabla}(\boldsymbol{\nabla}\cdot\mathbf{E}) + |\mathbf{E}|^2\mathbf{E} = \mathbf{0}. \tag{2}$$

The dimensionless parameter α in Eq. (1) is given by $\alpha = c^2/3v_e^2$, where c is the velocity of light and v_e is the mean electron thermal velocity. Since α contains a factor of c^2 in the numerator, it is quite large in typical situations. Indeed, its value ranges from about 20 for laboratory plasmas to about 2×10^5 for interstellar gas [2].

We are interested in this paper in collapsing solutions. The usual approach to the problem of proving blow-up for the nonlinear Schrödinger equation and related systems is to analyze the time evolution of the variance $V(t) = \int |\mathbf{x}|^2|\mathbf{E}|^2 d\mathbf{x}$. In the vector case, a general variance identity can be established [3],

$$\frac{d^2}{dt^2}\left(V(t) + 2(1-\alpha)\int_0^t \int x_i \,\mathrm{Im}[E_i \partial_j \overline{E_j}]\right)$$

$$= 4\alpha\left(2H - \frac{d-2}{2}\int |\mathbf{E}|^4\right), \tag{3}$$

where

$$H = \int \left(\alpha|\boldsymbol{\nabla}\mathbf{E}(t)|^2 + (1-\alpha)|\boldsymbol{\nabla}\cdot\mathbf{E}(t)|^2 - \tfrac{1}{2}|\mathbf{E}(t)|^4\right) \tag{4}$$

is the Hamiltonian.

In the special case $\alpha = 1$, it yields a blow-up result for initial conditions with a negative Hamiltonian [4]. However, for $\alpha \neq 1$ the modified variance no longer has a fixed sign and existence of blow-up solutions is not proved. We thus investigated this question numerically, by performing a series of simulations with various values of α. It is worth noticing that in two dimensions, there is a symmetry between solutions corresponding to reciprocal values of α. If $\mathbf{E} = (E_1(x_1,x_2,t), E_2(x_1,x_2,t))$ is a solution to Eq. (2) corresponding to some α, then the function

$$\mathbf{E}'(x_1,x_2,t) = (E_1(\sqrt{\alpha}x_2, \sqrt{\alpha}x_1, t), -E_2(\sqrt{\alpha}x_2, \sqrt{\alpha}x_1, t)) \tag{5}$$

is a solution corresponding to α^{-1}.

In view of characterizing the limiting profiles of the blow-up solutions, we started in Sec. II by computing the ground state (bound state solution of minimal action) of the corresponding problem

$$\alpha\Delta\mathbf{R} + (1-\alpha)\boldsymbol{\nabla}(\boldsymbol{\nabla}\cdot\mathbf{R}) - \mathbf{R} + |\mathbf{R}|^2\mathbf{R} = \mathbf{0}. \tag{6}$$

We numerically constructed ground states in two and three dimensions for a range of values of α. We then performed a series of simulations of the VNLS equation with various values of α. In dimension 2, for values of α close or equal to 1, we observed that the blow-up properties of the solution are similar to those of solutions of the critical scalar NLS equation. We also observed that the asymptotic profile of the solution near the point of blow-up resembles the ground state $\mathbf{R}$ up to rescaling (Sec. III). The calculations were well handled by the method of dynamic rescaling [3]. In the course of these simulations, for values of α small compared to one, we encountered the phenomenon of splitting, in which a solution with an initially single-peaked profile divides into two separate peaks as its amplitude increases.To overcome this difficulty, we implemented in Sec. IV a modified version of the iterative grid distribution method introduced in Ref. [5]. Our method avoids the iterative procedure. It consists of picturing the mesh as a grid of weighted nodes connected by springs. Each spring exerts a force on the two nodes at its end points, which is given in magnitude in terms on the spring tension k and the distance between the nodes.

*Electronic address: coleman@math.toronto.edu
†Electronic address: sulem@math.toronto.edu

Each node has a positive weight associated with it. The tension constant associated with each spring is defined as the arithmetic average of the weights of the two nodes that it connects. This leads to the construction of a curvilinear mesh that adapts dynamically to the function as it evolves by concentrating mesh points near regions of high amplitude. In Sec. V we apply this method to the VNLS equation in situations where splitting occurs. For small values of α, we observe that blow-up occurs at two points, and that the profile near these points is well-described by the ground state up to rescaling. We also consider the limiting case $\alpha=0$ in which blow-up appears to take a different form. In this case, the gradient norm $|\nabla \mathbf{E}|_{L^2}$ blows up, but the divergence norm $|\nabla\cdot\mathbf{E}|_{L^2}$ remains bounded, while the amplitude increases very slowly and possibly saturates. In Sec. VI, we finally apply our method to the time dispersion NLS equation associated with the propagation of ultrashort pulses passing through a nonlinear medium. Previous computations [6] have suggested that the normal time dispersion term can cause multisplitting and a saturation of the amplitude. We confirm these observations and compute the profiles of the solution.

II. NUMERICAL SIMULATION OF STANDING-WAVE SOLUTIONS

We are interested in solutions of the VNLS equation in the form of standing-wave solutions

$$\mathbf{E}(\mathbf{x},t)=\exp(it)\mathbf{R}(\mathbf{x}), \tag{7}$$

where $\mathbf{R}$ solves

$$\alpha\Delta\mathbf{R}+(1-\alpha)\nabla(\nabla\cdot\mathbf{R})-\mathbf{R}+|\mathbf{R}|^2\mathbf{R}=\mathbf{0}. \tag{8}$$

Existence of a solution of Eq. (8) as a minimizer for some functional is shown in Ref. [7] (see Ref. [8] for a detailed proof) using methods of concentration compactness. The problem of uniqueness (up to the family of gauge transformations under which this equation is invariant) appears to be quite difficult and at present it is still an open question. The bound state equation (6) is a nonlinear, vector-valued elliptic boundary value problem. For the corresponding scalar problem with $\alpha=1$, one knows that solutions are radially symmetric [9]. The equation then reduces to

$$R''+\frac{d-1}{r}R'-R+R^3=0,\quad R'(0)=0,\quad R(\infty)=0. \tag{9}$$

This problem can be solved numerically by a shooting method, as done, for example, in Refs. [10,11] in a more general context.

For the vector case, since solutions are no longer radial one must work in the full space $\mathbb{R}^d$ (or at least in a sufficiently large d-dimensional box). The method that we describe here is based on an iterative procedure that begins with an initial guess and converges rapidly to an exact solution. Equation (6) is invariant under phase shifts, rotations, and translations. The three degrees of freedom associated with these invariances can be eliminated if we specify that solutions to Eq. (6) must satisfy the normalization conditions

$$\mathbf{E}(\mathbf{0})=(\lambda,0,\ldots,0),\qquad \int \mathbf{x}|\mathbf{E}(\mathbf{x})|^2 d\mathbf{x}=\mathbf{0}, \tag{10}$$

where $\lambda>0$. The first equation specifies the choice of θ and O, while the second specifies the choice of $\mathbf{x}$ by requiring that the center of mass of $\mathbf{E}$ be located at the origin. Note that Eq. (10) implicitly assumes that bound states do not vanish at their center of mass. All of the bound states that we construct satisfy this property.

We now describe the method in detail. Fixing $\alpha>0$, we look for a solution $\mathbf{E}$ to $F(\mathbf{E})=\mathbf{0}$, where

$$F(\mathbf{E})=\alpha\Delta\mathbf{E}+(1-\alpha)\nabla(\nabla\cdot\mathbf{E})-\mathbf{E}+|\mathbf{E}|^2\mathbf{E}, \tag{11}$$

which satisfies Eq. (10). We construct this function through the method of quasilinearization, by defining a series of approximants $\mathbf{E}_0,\mathbf{E}_1,\mathbf{E}_2,\ldots$, which converge to a solution $\mathbf{E}$. If $\mathbf{E}_k$ is one such approximant and we set $\mathbf{e}_k=\mathbf{E}-\mathbf{E}_k$, then to leading order $\mathbf{e}_n$ satisfies $L_k(\mathbf{e}_k)=F(\mathbf{E}_k)$, where

$$L_k(\mathbf{e})=\alpha\Delta\mathbf{e}+(1-\alpha)\nabla(\nabla\cdot\mathbf{e})-\mathbf{e}+3|\mathbf{E}_k|^2\mathbf{e}. \tag{12}$$

This motivates the following iterative method. We begin by choosing some initial estimate $\mathbf{E}_0$, and we then define a sequence of functions recursively by $\mathbf{E}_k=\mathbf{E}_{k-1}+\mathbf{e}_{k-1}$ for $k\geqslant 1$, where $\mathbf{e}_{k-1}$ is determined from Eq. (12). We iterate this process until for some k we have $|\mathbf{e}_k|_{L^\infty}<\epsilon$, where ϵ is some fixed tolerance. At this point $\mathbf{E}_k$ has essentially converged to a fixed point, which we take to be the desired solution $\mathbf{E}$.

The linearized differential equation $L_k(\mathbf{e}_k)=F(\mathbf{E}_k)$ is discretized using a finite difference method. We work on the domain $D=[-L,L]^d\subset\mathbb{R}^d$, where L is chosen to be sufficiently large, and use as approximate boundary conditions that $\mathbf{E}=\mathbf{0}$ on ∂D. The differential operators are approximated by a seven-point scheme in each direction (accurate to sixth order in $h=L/n$, where n is the number of points in each direction), and at the boundary are calculated by extrapolating to fictitious points outside D where $\mathbf{e}_n$ is assumed to vanish identically. The resulting linear system has the form $A\mathbf{x}=\mathbf{b}$, where $\mathbf{x}$ and $\mathbf{b}$ are vectors with $N=(2n-1)^d$ elements, and A is a sparse positive matrix with N^2 elements. This system is solved by the conjugate-gradient method.

We now consider the problem of choosing an initial estimate $\mathbf{E}_0$. For $\alpha=1$, the ground state that satisfies Eq. (10) is given by $\mathbf{R}=(R,0,\ldots,0)$, where R is the ground state for the scalar NLS equation. To find $\mathbf{E}_0$ for $\alpha\neq 1$, we make the assumption that $\mathbf{R}$ varies continuously as a function of α. Hence, for values close to one, we take $\mathbf{E}_0=(R,0,\ldots,0)$. We found experimentally that this approximation is valid, indeed for all $0.5\leqslant\alpha\leqslant 2.0$ the iterative process converged to an exact numerical solution. By using a continuation process, we can extend our results to a large range of values of α.

A. Ground states in two dimensions

In this section we study the properties of the ground states computed for $d=2$. We used seven different values for α, ranging from 0.1 to 10.0. For all values of α we used $n=100$, while for L we used values that varied between 5 and 15 depending on the value of α. In Table I, we have listed

TABLE I. Properties of the numerically computed ground state **R** for $d=2$.

	R_1			R_2			**R**
α	min	max	L^2 norm	min	max	L^2 norm	L^2 norm
0.1	−0.063	2.349	1.495	−0.357	0.357	0.489	1.573
0.2	−0.018	2.284	1.999	−0.281	0.281	0.493	2.059
0.5	0	2.222	2.798	−0.139	0.139	0.321	2.816
1.0	0	2.206	3.421	0	0	0	3.421
2.0	0	2.222	3.957	−0.139	0.139	0.455	3.983
5.0	−0.018	2.284	4.471	−0.281	0.281	1.102	4.605
10.0	−0.063	2.351	5.670	−0.357	0.357	1.855	5.966

the minimum and maximum values and the L^2 norm for both components R_1 and R_2 of **R**. In Fig. 1, we show surface plots of these functions for two values of α, $\alpha=0.1$ and $\alpha=5$.

For $\alpha=1$, we obtained a maximum amplitude of 2.206, which is in agreement to three decimal places with the known value computed in the scalar case.

For $\alpha<1$, we observe that the contours of R_1 are roughly elliptical, with the major axis of the ellipse aligned along the x_1 axis and the minor axis along the x_2 axis. As α decreases towards zero, these contours become more elongated, and eventually assume a dipolelike structure. For all values of α sufficiently close to one, R_1 is strictly positive, however, as α decreases it eventually develops a pair of minima at the points $(0,\pm c)$ (where $c>0$ depends on α), at which it assumes a negative value. The threshold value of α for the onset of this behavior appears to be near 0.2. For R_2 we observe local maxima in the first and third quadrants, and local minima in the second and fourth quadrants having a magnitude that increases as α moves away from 1. Finally, as α tends to zero we find that both R_1 and R_2 became more concentrated near the origin. A similar pattern was observed for $\alpha>1$. Finally, we note that there is a symmetry between ground states corresponding to reciprocal values of α. Indeed, if $\mathbf{R}=(R_1,R_2)$ is a ground state corresponding to a particular value of α, then the ground state $\mathbf{R}'$ for α^{-1} is given by

$$\mathbf{R}'(x_1,x_2)=(R_1(\sqrt{\alpha}x_2,\sqrt{\alpha}x_1),-R_2(\sqrt{\alpha}x_2,\sqrt{\alpha}x_1)). \tag{13}$$

This is of course to be expected in view of the invariance (5).

The importance of these results lies in the relation with the structure of blow-up solutions. Indeed, we will show numerically in Secs. III B and IV A that, in two dimensions, the asymptotic profile of solutions near the blow-up point(s) is the ground state (up to scaling factors). This extends the results observed for the scalar NLS equation to the vector case.

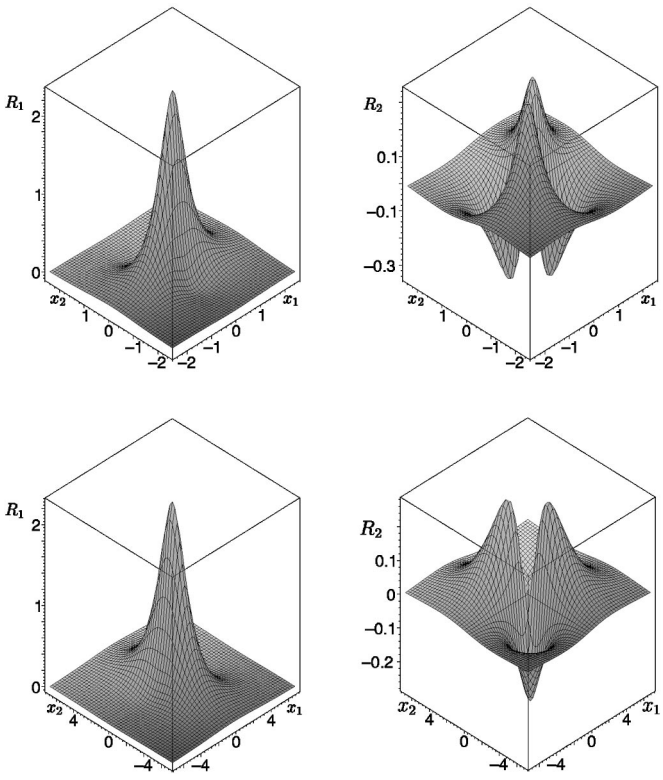

FIG. 1. Surface plots of R_1 (left) and R_2 (right); top $\alpha=0.1$, bottom $\alpha=5.0$.

B. Ground states in three dimensions

We used five different values for α, ranging from 0.2 to 5.0. For all values of α we used $n=80$, while for L we used values that varied between 4 and 8 depending on the value of α.

In Fig. 2 we show contour plots of the amplitude of **R** for $\alpha=0.2$ in both the longitudinal direction (a cross-sectional view in the x_1-x_2 plane, or equivalently in any plane containing the x_1 axis), and in the transverse direction (a cross-sectional view in the x_2-x_3 plane).

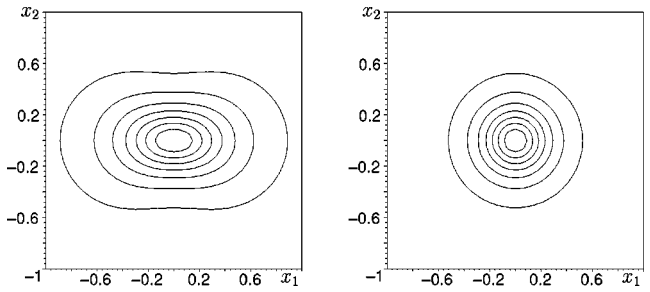

FIG. 2. Contour plots of ground state amplitude $|\mathbf{R}|$ for $d=3$ and $\alpha=0.2$.

TABLE II. Properties of the numerically computed ground state **R** for $d=3$.

	R_1			R_2			R_3		
α	min	max	L^2 norm	min	max	L^2 norm	min	max	L^2 norm
0.2	−0.004	4.536	1.568	−0.370	0.370	0.329	−0.370	0.370	0.329
0.5	0	4.390	2.922	−0.212	0.212	0.318	−0.212	0.212	0.318
1.0	0	4.338	4.345	0	0	0	0	0	0
2.0	0	4.417	5.758	−0.275	0.275	0.729	−0.275	0.275	0.729
5.0	−0.098	4.742	6.997	−0.606	0.606	2.005	−0.606	0.606	2.005

Finally, we list in Table II the minimum and maximum values and L^2 norms of the three component functions. As expected, the components R_2 and R_3 vanish when $\alpha=1$. They increase in amplitude as α tends to 0 or to infinity. Notice as well that the symmetry between ground states corresponding to reciprocal values of α which we observed in the two-dimensional case does not hold in three dimensions.

III. SINGLE-PEAK SOLUTIONS

In order to study the asymptotic structure of blow-up solutions numerically, it is necessary to use a method that evolves dynamically so that it captures the structure of the solution near the blow-up point. One such method is dynamic rescaling [12,13] (see Ref. [3] for a review). We define the rescaled variables $(\mathcal{E},\xi,\tau)$ by

$$\mathcal{E}(\xi,\tau)=O(t)^T L(t)\mathbf{E}(\mathbf{x},t), \quad \xi=D^{-1}(t)[\mathbf{x}-\mathbf{x}_0(t)],$$

$$\tau=\int_0^t \frac{ds}{L^2(s)}. \tag{14}$$

$D(t)$ is a d-by-d matrix of the form $D(t)=O(t)\Lambda(t)$, with $O(t)$ an orthogonal matrix and $\Lambda(t)$ a diagonal matrix whose diagonal elements are $\lambda_i(t)$ $(i=1,\ldots,d)$. We take $\mathbf{x}_0$ to be the centroid of the $2p$ power of $|\mathbf{E}|$ for some $p\geqslant 1$, and we choose $D(t)$ and $L(t)$ such that

$$\frac{\int \xi_i\xi_j|\mathcal{E}(\xi)|^{2p}d\xi}{\int |\mathcal{E}(\xi)|^{2p}d\xi}=\delta_{ij}, \quad \frac{d}{L^2(t)}=\sum_{i=1}^{d}\frac{1}{\lambda_i^2(t)}. \tag{15}$$

$\mathcal{E}$, λ_i, $\mathbf{x}_0$, and O satisfy the following system of equations:

$$i\left(\mathcal{E}_\tau+\frac{L_\tau}{L}\mathcal{E}+G\mathcal{E}+\mathbf{f}\cdot\boldsymbol{\nabla}\mathcal{E}\right)+\alpha\Delta_\Lambda\mathcal{E} +(1-\alpha)\Gamma_\Lambda\mathcal{E}+|\mathcal{E}|^2\mathcal{E}=\mathbf{0}, \tag{16}$$

$$\frac{d\lambda_i}{d\tau}=-a_{ii}\lambda_i, \quad i=1,\ldots,d, \tag{17}$$

$$\frac{d\mathbf{x}_0}{d\tau}=2O^T\Lambda\beta, \quad \frac{dO}{d\tau}=-GO. \tag{18}$$

In Eq. (16), the scalar and tensor differential operators Δ_Λ and Γ_Λ are given by

$$\Delta_\Lambda=L^2\Lambda^{-2}:\boldsymbol{\nabla}\boldsymbol{\nabla}, \quad \Gamma_\Lambda=L^2\Lambda^{-1}\boldsymbol{\nabla}\boldsymbol{\nabla}\Lambda^{-1}. \tag{19}$$

Also, $G=(g_{ij})$ and $A=(a_{ij})$ are d-by-d matrices, $\mathbf{f}$ is a vector in $\mathbb{R}^d$, with

$$a_{ij}=\frac{p\int(\delta_{ij}-\xi_i\xi_j)|\mathcal{E}|^{2p-2}\mathrm{Im}[\alpha\mathcal{E}\cdot\Delta_\Lambda\bar{\mathcal{E}}+(1-\alpha)\mathcal{E}\cdot\Gamma_\Lambda\bar{\mathcal{E}}]d\xi}{\int|\mathcal{E}|^{2p}d\xi}, \tag{20}$$

$$g_{ii}=0, \quad g_{ij}=\frac{2\lambda_i\lambda_j}{\lambda_i^2-\lambda_j^2}a_{ij} \quad (i\neq j), \quad \mathbf{f}=B\xi-2\beta, \tag{21}$$

where $B=(b_{ij})$ is an d-by-d matrix, $\beta=(\beta_i)$ is a vector, whose elements are given by

$$b_{ii}=a_{ii}, \quad b_{ij}=\frac{2\lambda_j^2}{\lambda_j^2-\lambda_i^2}a_{ij} \quad (i\neq j), \tag{22}$$

$$\beta_i=\frac{p\int\xi_i|\mathcal{E}|^{2p-2}\mathrm{Im}[\alpha\mathcal{E}\cdot\Delta_\Lambda\bar{\mathcal{E}}+(1-\alpha)\mathcal{E}\cdot\Gamma_\Lambda\bar{\mathcal{E}}]d\xi}{\int|\mathcal{E}|^{2p}d\xi}. \tag{23}$$

TABLE III. Limiting value of a as a function of α and initial condition $\mathbf{E}_0$.

	$(\lambda,\mu)=(1,1)$	$(\lambda,\mu)=(1,2)$	$(\lambda,\mu)=(1,3)$
$\alpha=0.5$	0.905227	0.905223	
$\alpha=1.0$	0.917417	0.917417	0.917416
$\alpha=2.0$	0.899349	0.899349	0.899348
$\alpha=5.0$	0.851958	0.851958	0.851959

Notice that the equations for $\mathcal{E}$ and λ_i decouple from the equations for $\mathbf{x}_0$ and O.

The numerical domain is the cube $[-L,L]^d$ with some sufficiently large L, and the interval $[0,L]$ is divided into n equal subdivisions. The spatial differential operators are discretized using finite differences, and a classical fourth-order Runge-Kutta scheme is used for time integration. Spatial integrals are calculated using Simpson's method.

A. Single-point blow-up in three dimensions

In this section, we consider the VNLS equation in three dimensions. For all of the simulations, we used parameters $L=10$, $n=30$, and $p=3$, and discretized the spatial differential operators using a five-point scheme. We performed simulations with four different values of α, namely, $\alpha=0.5$, $\alpha=1.0$, $\alpha=2.0$, and $\alpha=5.0$. For each of these values, we used initial conditions

$$\mathbf{E}_0(x_1,x_2,x_3)=6\exp\left(-x_1^2-\frac{x_2^2}{\lambda^2}-\frac{x_3^2}{\mu^2}\right)(1,0,0), \quad (24)$$

with $(\lambda,\mu)=(1,1)$, $(\lambda,\mu)=(1,2)$, and $(\lambda,\mu)=(1,3)$.

As $t\to t^*$ (or the rescaled time τ goes to ∞), the rescaled solution $\mathcal{E}$ stabilizes to the form

$$\mathcal{E}(\xi,\tau)\sim\exp(i\omega\tau)\hat{\mathcal{E}}(\xi), \quad \hat{\mathcal{E}}(\mathbf{0})=(c,0,0), \quad c>0, \quad (25)$$

where also the limiting frequency ω given by

$$\omega=\lim_{\tau\to\infty}\frac{1}{|\mathcal{E}(\mathbf{0},\tau)|^2}\mathrm{Im}\left[\frac{d\mathcal{E}(\mathbf{0},\tau)}{d\tau}\cdot\overline{\mathcal{E}(\mathbf{0},\tau)}\right], \quad (26)$$

stabilizes. The limiting value

$$a=-\lim_{\tau\to\infty}\frac{L_\tau}{\omega L}=\lim_{\tau\to\infty}\frac{L^2}{3\omega}\left(\frac{a_{11}}{\lambda_1^2}+\frac{a_{22}}{\lambda_2^2}+\frac{a_{33}}{\lambda_3^2}\right) \quad (27)$$

is computed for each simulation and is presented in Table III. Note that it is independent of the initial condition, and that for $\alpha=1$ it is equal to 0.9174 . . . , in excellent agreement with the value obtained in the scalar case [12].

No value is given for $\alpha=0.5$ and $(\lambda,\mu)=(1,3)$. This reflects the fact that in this case the simulation broke down due to the onset of splitting, a phenomenon in which an initially single-humped profile divides into two separate peaks as its amplitude increases. The dynamic rescaling method in its current form was unable to calculate the limiting behavior of such solutions. They will be investigated further in Sec. IV A, in the two-dimensional case, with a different method.

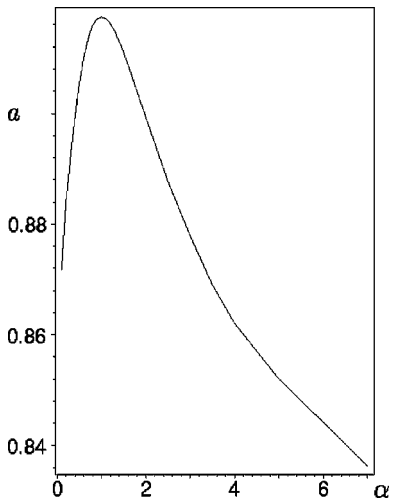

FIG. 3. Limiting value of $a=-LL_t$ as a function of α.

To determine the nature of the dependence of the blow-up rate on the parameter α, we ran a series of simulations for a large range of values of α using an initial condition $\mathbf{E}_0$ corresponding to $(\lambda,\mu)=(1,1)$, and calculated a in each case using Eq. (27). In Fig. 3, we plot the observed value of a against α. Notice that a attains its maximum value at $\alpha=1$. Referring to Eq. (14), we rewrite Eq. (25) in terms of the physical coordinates $\mathbf{x}$, t, and $\mathbf{E}$ as

$$\mathbf{E}(\mathbf{x},t)\sim\frac{1}{\sqrt{2a(t^*-t)}}e^{(i/2a)\ln([t^*/t^*-t])}\mathbf{A}\left(\frac{\mathbf{x}}{\sqrt{2a(t^*-t)}}\right), \quad (28)$$

where $\mathbf{A}$ should identify with a solution of

$$\alpha\Delta\mathbf{A}+(1-\alpha)\nabla(\nabla\cdot\mathbf{A})+ia(\mathbf{A}+(\mathbf{x}\cdot\nabla)\mathbf{A})+|\mathbf{A}|^2\mathbf{A}=\mathbf{0}, \quad (29)$$

with a given by the observed rate computed in Eq. (27). Figure 4 shows the contour plots of $|\mathbf{A}|$ for $\alpha=5$. On the left

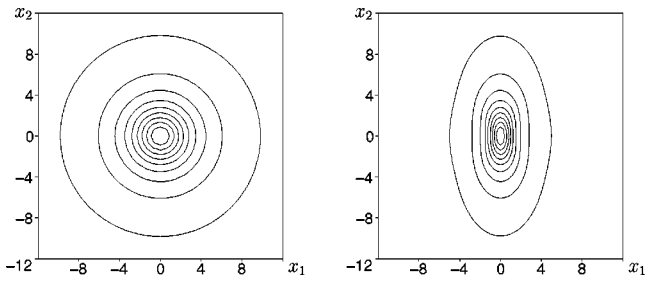

FIG. 4. Contour plots of rescaled profile $|\mathbf{A}|$ for $d=3$ and $\alpha=5.0$.

TABLE IV. Limiting value of $\lambda(\tau)$ for various values of α.

	$\tau_{\max}$	A	B	C	χ
$\alpha=0.5$	4000	3.28	3.90×10^{2}	-3.07×10^{5}	8.4×10^{-7}
$\alpha=1.0$	2000	3.19	1.02×10^{2}	-2.86×10^{4}	3.7×10^{-7}
$\alpha=2.0$	1000	3.13	4.11×10^{1}	-4.86×10^{3}	3.4×10^{-7}
$\alpha=5.0$	400	2.97	8.68×10^{1}	-9.53×10^{3}	2.7×10^{-6}

of the figure, we show a transverse view (a cross-sectional view in the x_2-x_3 plane), while on the right we show a longitudinal view (a cross-sectional view in the x_1-x_2 or x_1-x_3 plane).

B. Single-point blow-up in two dimensions

We now turn to the two-dimensional case. We used parameters $L=20$, $n=50$, and $p=3$, and we discretized the spatial differential operators using a seven-point scheme in each direction. We performed a series of simulations with four different values of α, namely, 0.5, 1.0, 2.0, and 5.0, with the initial condition

$$\mathbf{E}_0(x_1,x_2)=4\exp\left(-x_1^2-\frac{x_2^2}{\mu^2}\right)(1,0), \tag{30}$$

for $\mu=1$, $\mu=2$, and $\mu=3$. We were able to continue the simulations up to values of τ on the order of a thousand, at which time the amplitude of the solution in physical variables was greater than 10^{15}. Our results are very similar to those obtained for the scalar critical NLS equation. The solution stabilizes to the form

$$\mathcal{E}(\xi,\tau)=\exp[i\theta(\tau)]\hat{\mathcal{E}}(\xi,\tau),\quad \hat{\mathcal{E}}(\mathbf{0},\tau)=(c,0),\quad c>0, \tag{31}$$

where the profile $\hat{\mathcal{E}}$ varies extremely slowly. The angular frequency of $\mathcal{E}$ at the origin, computed as in the three-dimensional case, did not approach a limiting constant but rather continued to vary extremely slowly, consistent with a nearly self-similar behavior. We also compute the function $a(\tau)=-L_\tau/\omega L$. As expected, $a(\tau)$ was observed to decay extremely slowly to zero. In analogy with the scalar case, we assume a decay rate of the form

$$a(\tau)\sim\frac{\lambda}{\ln\tau+3\ln\ln\tau}, \tag{32}$$

with λ depending on α. The function $\lambda(\tau)=a(\tau)(\ln\tau+3\ln\ln\tau)$ converges extremely slowly to some value. To make this more precise, we fit this curve to the function $\lambda_{\text{approx}}(\tau)=A+B/\tau+C/\tau^2$, where the parameters A, B, and C are chosen to minimize

$$\chi=\sqrt{\frac{1}{n}\sum_{i=1}^{n}[\lambda_{\text{approx}}(\tau_i)-\lambda(\tau_i)]^2},$$

TABLE V. Comparison of L^2 and L^∞ norms of **A** and **R** for various values of α.

			R		**A**	
α	γ_1	γ_2	L^2 norm	L^∞ norm	L^2 norm	L^∞ norm
0.5	1.211	0.871	2.82	2.22	2.85	2.19
1.0	1.000	1.000	3.42	2.21	3.45	2.18
2.0	0.871	1.211	3.98	2.22	4.04	2.19
5.0	0.799	1.518	4.60	2.28	4.73	2.21

with τ_i a sequence of n values that tend to $\tau_{\max}$. The form of the function was chosen because it gave reasonable values for the parameters A, B, and C, and was relatively insensitive to the value of $\tau_{\max}$. Results for different values of α are shown in Table IV. For $\alpha=1$ we compute a limiting value of $A=3.19$, which is in good agreement with the theoretically predicted value $A=\pi$. The error term χ was quite small relative to the value $a=0.24$ at the end of the simulation, indicating that $\lambda_{\text{approx}}(\tau)$ is a close fit to $\lambda(\tau)$.

We now turn to the study of the limiting profile $\mathcal{E}$. Using Eq. (14) to convert from rescaled to physical coordinates, and eliminating ω by rescaling, we find that

$$\mathbf{E}(\mathbf{x},t)\sim\frac{1}{L(t)}\exp[i\theta(\tau(t))]\mathbf{A}\left(\frac{\mathbf{x}}{L(t)},\tau\right), \tag{33}$$

where

$$\mathbf{A}(\xi,\tau)=\frac{1}{\sqrt{\omega(\tau)}}\hat{\mathcal{E}}\left(\frac{\xi_1}{\gamma_1\sqrt{\omega(\tau)}},\frac{\xi_2}{\gamma_2\sqrt{\omega(\tau)}},\tau\right), \tag{34}$$

and the stretching factors γ_1 and γ_2 are given by

$$\gamma_1=\lim_{\tau\to\infty}\frac{\lambda_1(\tau)}{L(\tau)},\qquad \gamma_2=\lim_{\tau\to\infty}\frac{\lambda_2(\tau)}{L(\tau)}. \tag{35}$$

As expected, the limiting values of γ_1 and γ_2 were independent of $\mathbf{E}_0$; they are listed in Table V for different values of α. By analogy with the scalar case, we expect **A** to coincide with the ground state **R** corresponding to the value of α used in the simulation. We list in Table V the L^2 and L^∞ norms of **A** and **R**, which agree to within a few percent. The data for the ground states have been computed from the numerical results obtained in Sec. II A. As an example, we plot in Fig. 5 the level curves of $|\mathbf{A}|$ and $|\mathbf{R}|$ for $\alpha=0.5$.

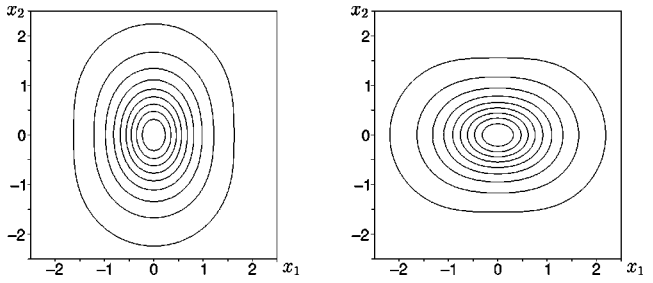

FIG. 5. Contour plots of $|\mathbf{A}|$ (left) and $|\mathbf{R}|$ (right) for $d=2$ and $\alpha=0.5$.

IV. TWO-POINT BLOW-UP FOR THE VNLS EQUATION

When performing simulations for values of α small compared to one, we encounter the phenomenon of splitting, in which a solution with an initially single-peaked profile divides into two separate peaks as its amplitude increases. To capture the dynamics, we use a numerical method that constructs a curvilinear mesh that adapts dynamically to the function as it evolves, by concentrating mesh points near regions of high amplitude. It is a structured mesh generation algorithm, and consists of constructing a time-dependent transformation that acts on the spatial domain D and maps the physical solution $\mathbf{E}$ to a logical solution $\mathcal{E}$. The number of nodes is fixed and their locations change as the solution evolves. The resulting mesh is nonuniform and, in particular, the mesh lines do not intersect orthogonally. A detailed description of the mesh refinement method can be found in Ref. [8]. In Appendix A, we briefly recall the main ideas.

A. The case $\alpha=0.1$

We apply mesh refinement technique to the cubic VNLS equation in two dimensions, where splitting of the profile has been observed for small values of the parameter α. We introduce logical variables $\mathcal{E}=(\mathcal{E}_1,\mathcal{E}_2)$ and $\xi=(\xi_1,\xi_2)$ and rewrite Eq. (2) in terms of the new variables and the coefficients a_{ij}^{kl} and b_{ij}^{k} listed in Appendix B to obtain the evolution equations

$$\frac{d\mathcal{E}_1}{dt}=i(c_1^{11}\partial_{11}\mathcal{E}_1+c_1^{12}\partial_{12}\mathcal{E}_1+c_1^{22}\partial_{22}\mathcal{E}_1+c_1^{1}\partial_{1}\mathcal{E}_1 + c_1^{2}\partial_{2}\mathcal{E}_1+d_1^{11}\partial_{11}\mathcal{E}_2+d_1^{12}\partial_{12}\mathcal{E}_2+d_1^{22}\partial_{22}\mathcal{E}_2 + d_1^{1}\partial_{1}\mathcal{E}_2+d_1^{2}\partial_{2}\mathcal{E}_2+|\mathcal{E}|^2\mathcal{E}_1), \tag{36}$$

$$\frac{d\mathcal{E}_2}{dt}=i(c_2^{11}\partial_{11}\mathcal{E}_2+c_2^{12}\partial_{12}\mathcal{E}_2+c_2^{22}\partial_{22}\mathcal{E}_2+c_2^{1}\partial_{1}\mathcal{E}_2 + c_2^{2}\partial_{2}\mathcal{E}_2+d_2^{11}\partial_{11}\mathcal{E}_1+d_2^{12}\partial_{12}\mathcal{E}_1+d_2^{22}\partial_{22}\mathcal{E}_1 + d_2^{1}\partial_{1}\mathcal{E}_1+d_2^{2}\partial_{2}\mathcal{E}_1+|\mathcal{E}|^2\mathcal{E}_2), \tag{37}$$

where

$$c_1^{ij}=a_{11}^{ij}+\alpha a_{22}^{ij},\quad c_1^{i}=a_{11}^{i}+\alpha a_{22}^{i},$$
$$c_2^{ij}=a_{22}^{ij}+\alpha a_{11}^{ij},\quad c_2^{i}=a_{22}^{i}+\alpha a_{11}^{i}, \tag{38}$$
$$d_1^{ij}=d_2^{ij}=2(1-\alpha)a_{12}^{ij},\quad d_1^{i}=d_2^{i}=2(1-\alpha)a_{12}^{i}.$$

The mesh refinement equations for x_1, x_2, and $\mathcal{E}$ are identical to those in the scalar case [see Eqs. (A6)–(A8)] with φ replaced by $\mathcal{E}$.

We begin by running a simulation with $\alpha=0.1$ and the initial condition

$$\mathbf{E}_0(x_1,x_2)=4\exp(-x_1^2-x_2^2)(1,0). \tag{39}$$

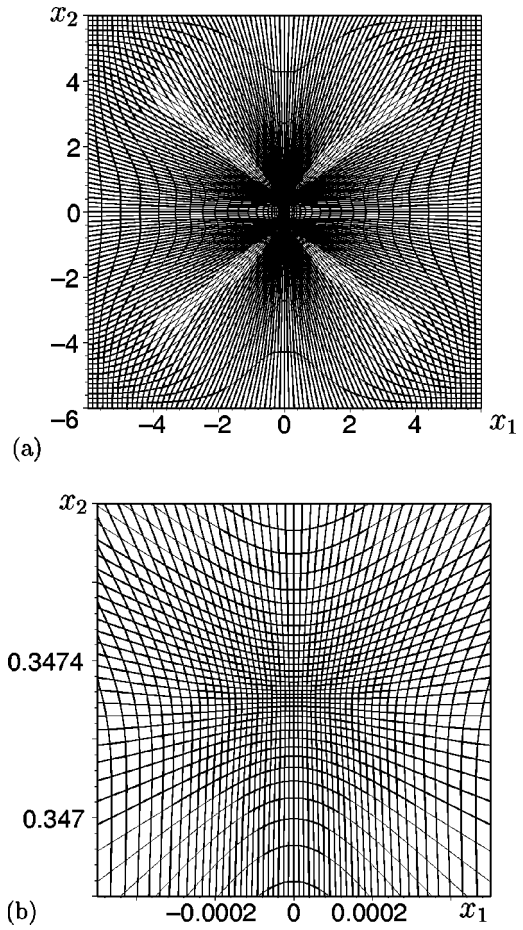

FIG. 6. Mesh plots for two-point blow-up of VNLS equation with $\alpha=0.1$ at end of simulation.

We use the parameters $L=6$, $n_1=n_2=120$, and $M=3$. For the weight functional we found that it was necessary to include higher derivative terms in order to keep the logical function $\mathcal{E}$ well behaved, and so we took

$$w(\mathbf{E})=S[(1+|\mathbf{E}|^6+0.1|\boldsymbol{\nabla}\boldsymbol{\nabla}\mathbf{E}|^2)^{1/6}], \tag{40}$$

with smoothing parameters [see Eq. (A13)] $s_1=s_2=12$. The incorporation of terms containing second derivatives of the function is particularly important for simulations in which the structure of the solution has a complex form.

The blow-up begins as in the scalar case, but after a short time the peak becomes elongated and two subpeaks form on either side of the main peak. These subpeaks gradually increase in magnitude, while the main peak diminishes. Eventually, $\mathbf{E}$ forms two distinct peaks at the points $(0,\pm c)$ with $c\approx 0.3473$, superimposed on a small shoulder component that surrounds the peaks and attains its maximum at the origin. The amplitude then increases extremely rapidly as a portion of the mass concentrates near each peak, while the remaining portion dissipates into the shoulder component. We were able to continue the simulation up to a rescaled time

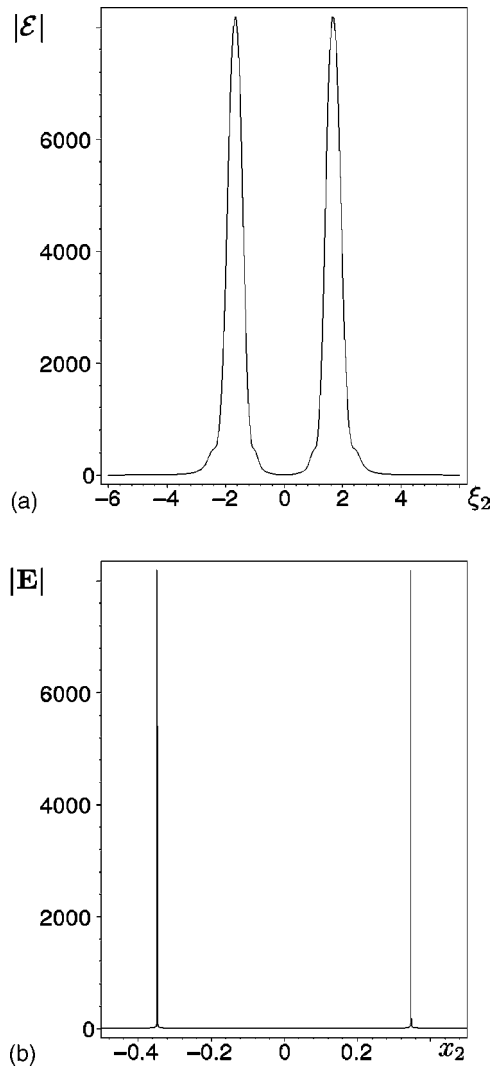

FIG. 7. Two-point blow-up solution of VNLS equation with $\alpha=0.1$ at the end of the simulation; (a) $|\mathcal{E}|$ along ξ_2 axis (logical coordinates); (b) $|\mathbf{E}|$ along the x_2 axis (physical coordinates).

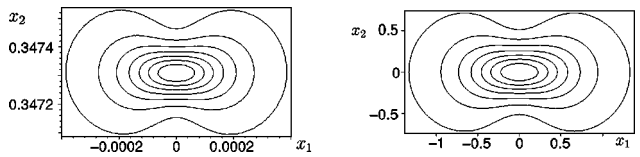

FIG. 9. Asymptotic form of two-point blow-up solution of the VNLS equation with $\alpha=0.1$.

$\tau=73.1$. At the end of the simulation the amplitude was approximately 8.2×10^3, while the physical time was approximately $t=0.358\,206$. The mesh points at the end of the simulation are plotted in Fig. 6. Profiles of the amplitude along the x_2 axis at the end of the simulation in both physical and logical variables are given in Fig. 7. In Fig. 8 we show the evolution of the amplitude, gradient, and divergence as a function of the rescaled time τ. We are also interested in studying the behavior of the profile of the solution near each peak close to the blow-up time. In Fig. 9 (left) we show a contour plot of $|\mathbf{E}|$ near one of the peaks at the end of the simulation, while at the right we show a contour plot of the amplitude $|\mathbf{R}|$ of the ground state corresponding to $\alpha=0.1$ (as computed in Sec. II A). These plots are seen to be identical up to a uniform spatial dilation.

B. The limiting case: $\alpha=0$

Since the splitting phenomenon for the VNLS equation appears to be correlated with small values of α, we next investigated the behavior in the limiting case $\alpha=0$. The equation with $\alpha=0$ (but including an additional cubic nonlinear term) also arises in modeling the dynamics of a small-amplitude Alfvén wave propagating in a plasma permeated by an ambiant magnetic field [14] (see also Ref. [15]).

In our calculations, we used the parameters $L=6$, $n_1=n_2=120$, tolerance $M=3$, and the weight functional

$$w(\mathbf{E})=S[(1+|\nabla\nabla\mathbf{E}|^2)^{1/6}], \tag{41}$$

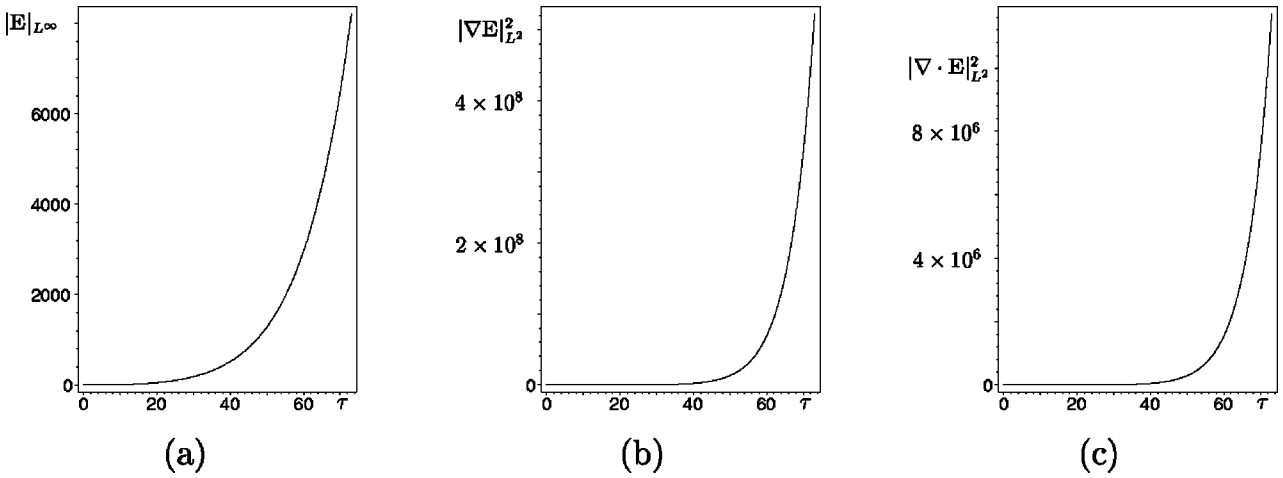

FIG. 8. Evolution of (a) $|\mathbf{E}|_{L^\infty}$, (b) $|\nabla\mathbf{E}|^2_{L^2}$, and (c) $|\nabla\cdot\mathbf{E}|^2_{L^2}$, as a function of τ for the VNLS equation with $\alpha=0.1$.

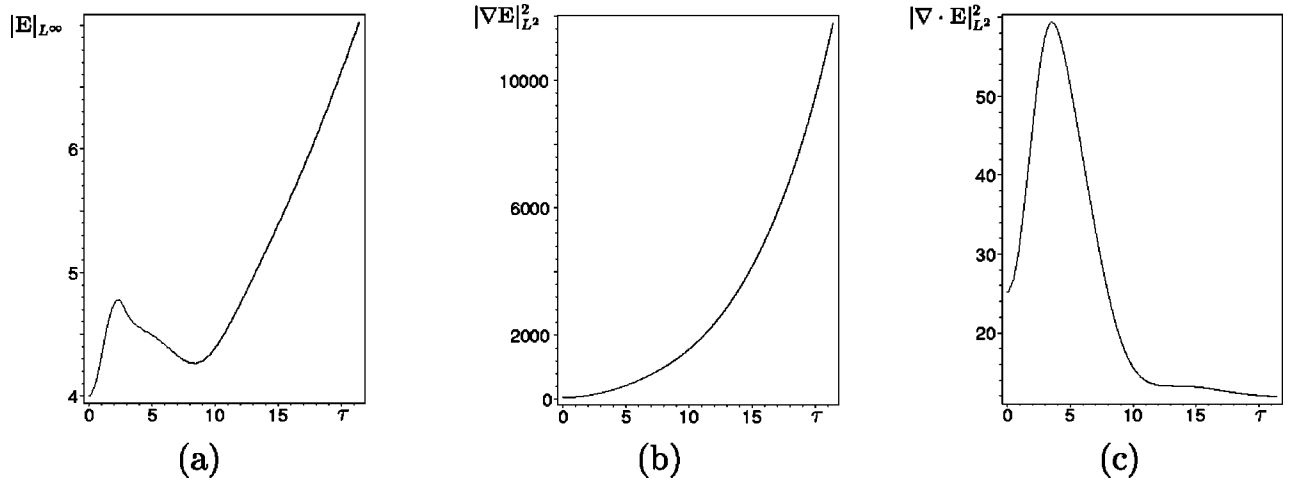

FIG. 10. Evolution of (a) $|\mathbf{E}|_{L^\infty}$, (b) $|\nabla \mathbf{E}|^2_{L^2}$, and (c) $|\nabla \cdot \mathbf{E}|^2_{L^2}$, as a function of τ, for the VNLS equation with $\alpha=0$.

with smoothing parameters $s_1=s_2=6$. The dynamics of the blow-up are different than those for $\alpha=0.1$. The amplitude begins to increase, and then almost immediately the profile splits into two peaks. Each of these peaks increases in amplitude very slowly, while the gradient increases much more rapidly. Eventually, two very sharp peaks with small amplitude are formed, as well as a number of cusps. The blow-up is characterized by a gradient very large relative to the amplitude of the solution. The time step refinement procedure causes the time-step to decrease rapidly, and it becomes impractical to continue the simulation beyond this point.

In Fig. 10 we plot the evolution of the amplitude, gradient, and divergence as a function of the rescaled time τ. Notice that although the gradient continues to increase as in the case where $\alpha=0.1$, the divergence actually decreases and appears to approach a limiting value. The amplitude increases extremely slowly and it is unclear whether or not it eventually saturates. In Fig. 11 we show profiles of the function along the x_2 axis at two points in the computation. On the left we show **E** in physical coordinates, while on the right we show the logical function $\mathcal{E}$. Notice that $\mathcal{E}$ remains fairly smooth even after **E** has become strongly peaked, although the resolution of the cusps was less effective than that of the peaks. Nonetheless, the accurate conservation of the energy (the maximum relative error was about 3×10^{-4}) suggests that the simulation is accurate.

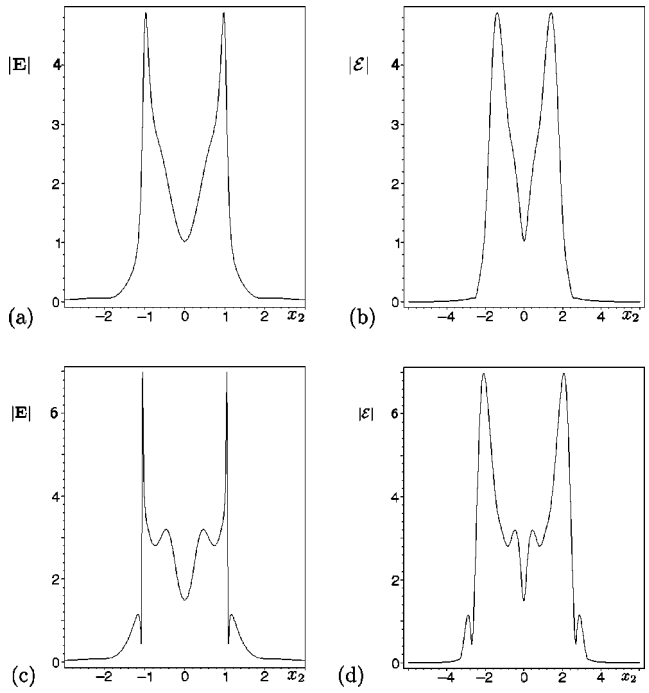

FIG. 11. Profiles of the solution of VNLS equation with $\alpha=0$ along the x_2 axis.

V. TIME DISPERSION NLS EQUATION

In this section, we apply the dynamic mesh refinement algorithm to study the problem of the time dispersion NLS equation (TDNLS)

$$iu_z+u_{xx}+u_{yy}-\epsilon^2 u_{tt}+|u|^2u=0, \tag{42}$$

which describes the motion of an ultrashort wave train emitted by a laser as it passes through a nonlinear medium.

We will restrict our study to radially symmetric solutions in the transverse plane. The dynamics of this problem have been studied by several authors both analytically [16,17], and numerically [3,18]. Numerical simulations show that the transverse focusing leads to splitting of the original pulse in the t direction, although further conclusions about the dynamics could not be established. Using an adaptive mesh refinement scheme, Germaschewski *et al.* [19] observed that, after the first spitting, each peak may undergo in some cases, sequential divisions near the outer edge of the pulse. Our calculations seem to confirm these observations as well as new computations by Fibich *et al.* [6]. Transforming from physical coordinates (u,r,t) to logical coordinates (φ,ρ,τ), Eq. (42) is rewritten in its radial form

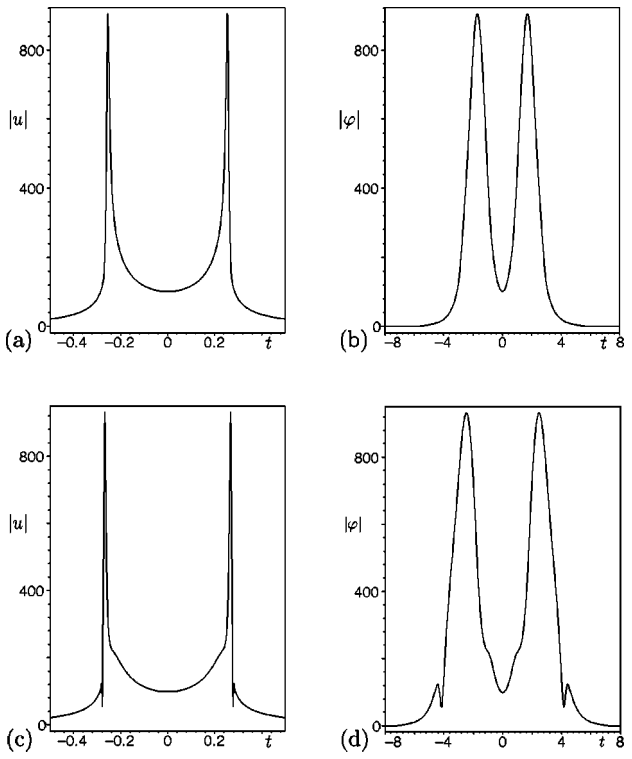

FIG. 12. Profiles of the solution of TDNLS equation along t axis for $\epsilon=1$ and $u_0=6\exp(-r^2-t^2)$.

$$\varphi_z = i\Big(\frac{1}{r(\rho,\tau)}(c_1\partial_\rho + c_2\partial_\tau)[c_1 r(\rho,\tau)\partial_\rho\varphi + c_2 r(\rho,\tau)\partial_\tau\varphi] - \epsilon^2(a_{22}^{11}\partial_{\rho\rho}\varphi + 2a_{22}^{12}\partial_{\rho\tau}\varphi + a_{22}^{22}\partial_{\tau\tau}\varphi + b_{22}^{1}\partial_\rho\varphi + b_{22}^{2}\partial_\tau\varphi) + |\varphi|^2\varphi\Big), \quad (43)$$

where

$$c_1 = \frac{1}{J}\frac{\partial t}{\partial \tau}, \quad c_2 = -\frac{1}{J}\frac{\partial t}{\partial \rho}, \quad J = \frac{\partial r}{\partial \rho}\frac{\partial t}{\partial \tau} - \frac{\partial r}{\partial \tau}\frac{\partial t}{\partial \rho}, \quad (44)$$

and a_{ij}^{kl} and b_{ij}^{k} are the coefficients given in Appendix A with x_1, x_2, ξ_1, and ξ_2 replaced by r, t, ρ, and τ, respectively.

We first considered the problem corresponding to $\epsilon=1$ with isotropic initial condition

$$u_0(r,t) = 6\exp(-r^2-t^2), \quad (45)$$

as studied in Sec. 9.2 of Ref. [3]. For our parameters we take $L=6, n_1=160, n_2=200, M=3$, and we use the weight functional

$$w(u) = S[(1+|\nabla\nabla u|^2)^{1/6}], \quad (46)$$

with smoothing parameters $s_1=16$ and $s_2=20$.

The dynamics of this problem are more complicated than those of previous simulations. As in the case of the VNLS equation with small α we observe splitting, but the onset of splitting is much more delayed. The solution begins to develop with a profile consisting of a single peak, which reaches an amplitude of about 150. This peak is extremely elongated in the t direction; indeed at this point the contours of $|u|$ are about 50 times as long in the t direction as in the r direction. Only at this point does splitting begin to occur, and two distinct peaks eventually form. Both of these peaks are also extremely elongated in the t direction. In addition to the main peaks, there are a series of local undulations in the cross-sectional profiles of the amplitude parallel to the t axis. These undulations gradually become more and more complicated, until finally a second splitting of the main peaks begins to occur. By this point the amplitude has saturated, after attaining a maximum of about 10^3, and begins to decrease gradually.

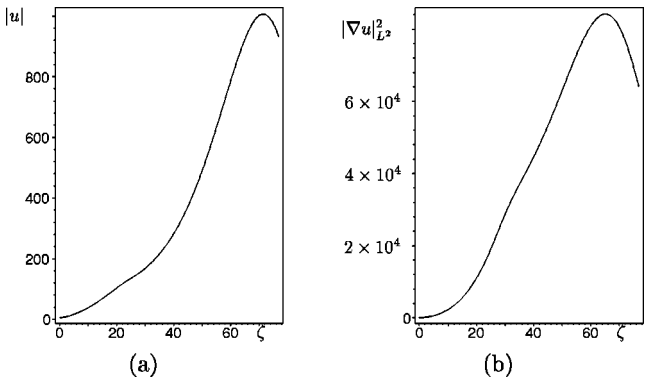

FIG. 13. Evolution of amplitude and square of the gradient of the L^2 norm for TDNLS equation for $\epsilon=1$ and $u_0=6\exp(-r^2-t^2)$ as a function of ζ.

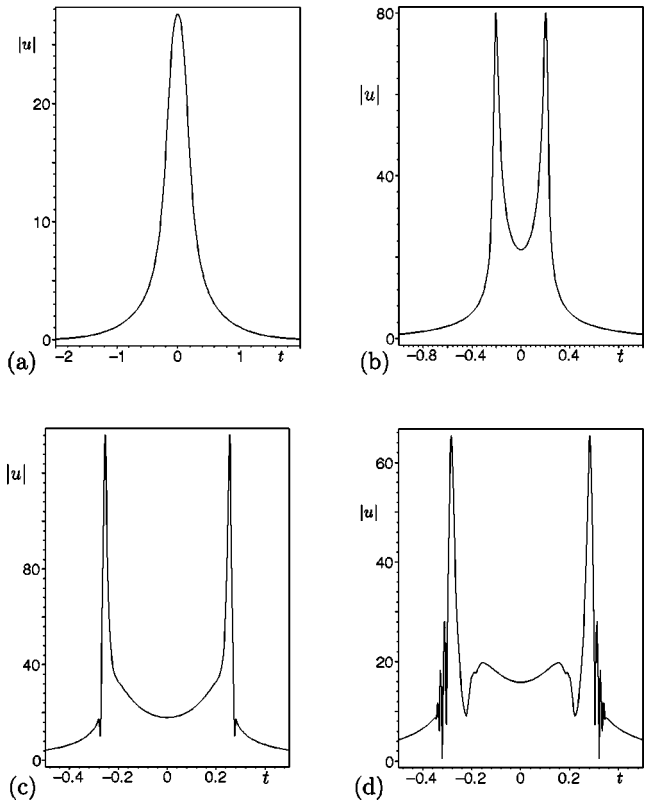

FIG. 14. Profile of $|u|$ along t axis for TDNLS equation for $\epsilon=\frac{1}{4}$ and $u_0=3.5\exp(-r^2-t^2)$.

In Fig. 12 we show profiles of the solution along the t axis for two values of z in both physical and logical coordinates. As can be seen, the mesh transformation is able to resolve the extremely high gradients associated with the shocks on either side of the main peaks. We also show in Fig. 13 the evolution of various quantities associated with the solution as a function of the rescaled distance ζ defined by $\zeta = \int_0^z |u(z')|_{L^\infty}^2 dz'$, and analogous to the rescaled time τ considered earlier.

Next, we consider the problem corresponding to $\epsilon = 0.25$ with initial condition $u_0(r,t) = 3.5\exp(-r^2 - t^2)$, which, up to rescaling, is identical to that studied in Ref. [18]. We use parameters $L=6, n_1=120, n_2=240, M=2.5$, and the same weight functional as before with $s_1=12$ and $s_2=24$. In Fig. 14 we show a series of profiles of $|u|$ for various values of z. As with the first simulation, the dynamics of this problem appear to be quite complicated. The blow-up begins with a Gaussian-like profile, which quickly becomes highly elongated in the t direction. In the region $r>0$, a splitting begins to form, which gradually penetrates the peak until it reaches the t axis. The amplitude then increases in a two-peaked profile, while further subdivision occurs away from the t axis. The rate of blow-up decreases until a saturation point is reached at an amplitude of about 143. The amplitude then begins to decrease and further subdivision of the peaks occurs, until eventually two shocks form outside the main peaks. As the amplitude continues to decrease, multiple shocks form and the dynamics become extremely complicated. At this point, however, the simulation is at the limit of its validity, and due caution should be exercised when interpreting these results.

ACKNOWLEDGMENTS

We benefited from stimulating discussions with R. Russell. We acknowledge support from NSERC Operating Grant No. OGP0046179.

APPENDIX A: A DYNAMIC MESH REFINEMENT TECHNIQUE

Suppose that $u: D = [-L,L]^2 \to \mathbb{C}$, and u vanishes on ∂D. We define logical coordinates $\xi = (\xi_1, \xi_2)$ on D, and map D onto itself by a smooth invertible transformation $(\xi_1,\xi_2) \leftrightarrow (x_1,x_2)$ and the logical function $\varphi: D \to \mathbb{C}$ by $\varphi(\xi) = u(x_1(\xi_1,\xi_2), x_2(\xi_1,\xi_2))$. The problem is how to construct the transformation so that φ is as well behaved as possible. A comprehensive overview of various approaches can be found in Refs. [20,21]. All these methods have in common the concept of a weight functional w, whose value provides some indication of the relative concentration of mesh points necessary in a region in order to model u accurately. For example, a simple choice for a weight function is $w = 1 + |u|^2$. An important class of algorithms is composed of those which define the transformation in terms of a variational problem (see Ref. [22] or Chap. 6 of Ref. [20]). One of the most useful, first proposed by Winslow [23] in the context of an adaptive finite element algorithm, is given by

$$I_W(\xi) = \int_D \frac{1}{w^2(\mathbf{x})} \sum_{i,j} \left(\frac{\partial \xi_i}{\partial x_j} \right)^2 d\mathbf{x}. \tag{A1}$$

One seeks functions $\xi_1(x_1,x_2)$ and $\xi_2(x_1,x_2)$ that minimize I_W subject to the constraints $\xi_i(x_1,x_2) = x_i$, $i=1,2$ on ∂D. For this purpose, one writes the associated Euler-Lagrange equations ($i=1,2$),

$$L_i(\xi_1,\xi_2) \equiv \frac{\partial}{\partial x_1}\left(\frac{1}{w^2(\mathbf{x})} \frac{\partial \xi_i}{\partial x_1} \right) + \frac{\partial}{\partial x_2}\left(\frac{1}{w^2(\mathbf{x})} \frac{\partial \xi_i}{\partial x_2} \right) = 0. \tag{A2}$$

The system (A2) has the form of a pair of elliptic equations for $\xi_1(x_1,x_2)$ and $\xi_2(x_1,x_2)$. A straightforward way to solve this system numerically is to consider the associated evolution equations $d\xi_i/ds = L_i(\xi_1,\xi_2)$ for which the solution to Eq. (A2) is a fixed point. To test the effectiveness of this method, Ren and Wang [5] performed a series of numerical simulations and also use the Winslow algorithm iteratively to integrate time-dependent equations that develop singularities in finite time.

Here, we develop an approach that incorporates some of the above ideas. Rather than proceeding from a variational approach, we picture the mesh as a grid of weighted nodes connected by springs, a concept also discussed in a different context in Ref. [24]. A detailed description of the method is given in Ref. [8]. Let the mesh consist of a rectangular grid of nodes $N_{i,j}$ situated at physical positions $\mathbf{x}_{i,j} = ((x_1)_{i,j}, (x_2)_{i,j})$ in which each node is connected to its four closest neighbors by a spring. Each spring exerts a force on the two nodes at its end points, which is given in magnitude by the spring tension k multiplied by the distance between the nodes, and directed along the line of the spring. The constant k is different for each spring, and is determined as follows. Each node $N_{i,j}$ has associated with it a positive weight $w_{i,j} = w(x_{ij})$ where w is a weight function. The tension constant associated with each spring is then defined to be the arithmetic average of the weights of the two nodes that it connects. For example, the spring connecting node $N_{i,j}$ to node $N_{i+1,j}$ exerts a force

$$\mathbf{F} = \frac{1}{2}(w_{i,j} + w_{i+1,j})(\mathbf{x}_{i+1,j} - \mathbf{x}_{i,j}) \tag{A3}$$

on node $N_{i,j}$, and an equal and opposite force on node $N_{i+1,j}$. If the mesh is to be in equilibrium, then the net force on each node from the four springs attached to it must vanish; in other words, we must have

$$\begin{aligned}(w_{i,j} + w_{i+1,j})(\mathbf{x}_{i+1,j} - \mathbf{x}_{i,j}) + (w_{i,j} + w_{i-1,j})(\mathbf{x}_{i-1,j} - \mathbf{x}_{i,j}) \\ + (w_{i,j} + w_{i,j+1})(\mathbf{x}_{i,j+1} - \mathbf{x}_{i,j}) \\ + (w_{i,j} + w_{i,j-1})(\mathbf{x}_{i,j-1} - \mathbf{x}_{i,j}) = \mathbf{0}.\end{aligned} \tag{A4}$$

Now expand all of the quantities above in a second-order Taylor expansion about the node $N_{i,j}$. Equating coefficients of h^2, and separating into x_1 and x_2 components, we get the pair of equations ($i=1,2$)

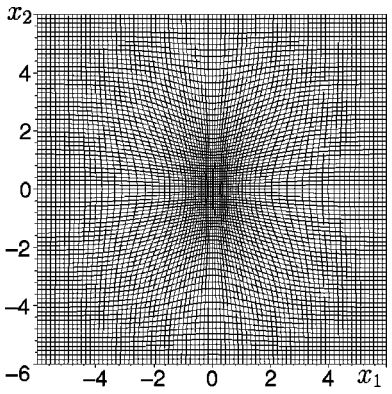

FIG. 15. Curvilinear mesh induced by u.

$$L_i(x_1,x_2)\equiv\frac{\partial^2 x_i}{\partial\xi_1^2}+\frac{\partial^2 x_i}{\partial\xi_2^2}+\frac{2}{w}\left(\frac{\partial w}{\partial\xi_1}\frac{\partial x_i}{\partial\xi_1}+\frac{\partial w}{\partial\xi_2}\frac{\partial x_i}{\partial\xi_2}\right)=0. \tag{A5}$$

To solve Eq. (A5), we consider the evolution equations for x_1, x_2, and φ in the form

$$\frac{dx_i}{ds}=L_i(x_1,x_2), \tag{A6}$$

$$\frac{d\varphi}{ds}=X_1\frac{\partial\varphi}{\partial\xi_1}+X_2\frac{\partial\varphi}{\partial\xi_2}, \tag{A7}$$

where

$$X_1=\frac{1}{J}\left(\frac{\partial x_2}{\partial\xi_2}\frac{dx_1}{ds}-\frac{\partial x_2}{\partial\xi_1}\frac{dx_2}{ds}\right),$$

$$X_2=\frac{1}{J}\left(\frac{\partial x_1}{\partial\xi_1}\frac{dx_2}{ds}-\frac{\partial x_1}{\partial\xi_2}\frac{dx_1}{ds}\right), \tag{A8}$$

and J is the Jacobian of the mapping $(\xi_1,\xi_2)\to(x_1,x_2)$. These equations are similar to the moving-mesh equations developed in Refs. [25,26]. Also, it follows from Eq. (A8) that

$$\frac{dx_i}{ds}=X_1\frac{\partial x_i}{\partial\xi_1}+X_2\frac{\partial x_i}{\partial\xi_2}. \tag{A9}$$

Equations (A7) and (A9) constitute a set of three first-order equations for x_1,x_2, and φ, and clearly all have the same characteristic curves in $D\times[0,\infty]$.

To visualize the method, we consider an example of mesh generation. Let $D=[-6,6]^2$ with a $2n$-by-$2n$ grid ($n=120$), and the test function be given by $u(x_1,x_2)=4\exp(-x_1^2-x_2^2/4)$. We construct a transformation, that induces physical coordinate functions $x_i(\xi_1,\xi_2)$ on D. Each of the regularly spaced mesh points $\xi_{i,j}$ is mapped to a new mesh point $\mathbf{x}_{i,j}$, and this new set of mesh points defines a curvilinear mesh on D which is adapted to the function u, as in Fig. 15.

We now extend the static mesh generation scheme to a method suitable for solving dynamical equations. One approach is to incorporate the time evolution directly into the mesh evolution equations. Such methods are known as moving mesh methods and are discussed in detail in Refs. [25–27]. A second approach, taken in this work, is to decouple the time-dependent problem into two steps, one in which the mesh is fixed and the solution evolves in time, and the second in which time is held fixed and a static mesh generation scheme is applied to the current value of the solution.

Let us illustrate it on a model problem, the critical NLS equation in two dimensions,

$$\frac{du}{dt}=i\left(\frac{\partial^2 u}{\partial x_1^2}+\frac{\partial^2 u}{\partial x_2^2}+|u|^2u\right), \tag{A10}$$

with initial condition $u(\mathbf{x},0)=u_0(\mathbf{x})=4\exp(-|\mathbf{x}|^2)$. At $t=0$, we initialize the mesh transformation to the identity, and $\varphi=u_0$. The method consists of alternating between evolution and mesh generation phases. During the evolution phase, the $x_i(\xi_1,\xi_2)$ are held constant, and u is allowed to evolve in time. The evolution equations are determined by rewriting the spatial derivatives appearing in Eq. (A10) in terms of ξ_1 and ξ_2:

$$\frac{\partial^2 u}{\partial x_i\partial x_j}=\sum_{k,l}a_{ij}^{kl}\frac{\partial^2\varphi}{\partial\xi_k\partial\xi_l}+b_{ij}^k\frac{\partial\varphi}{\partial\xi_k}. \tag{A11}$$

The coefficients a_{ij}^{kl} and b_{ij}^k are calculated in Appendix B. Substituting Eq. (A11) into Eq. (A10) we obtain the evolution equation

$$\frac{d\varphi}{dt}=i[(a_{11}^{11}+a_{22}^{11})\partial_{11}\varphi+2(a_{11}^{12}+a_{22}^{12})\partial_{12}\varphi+(a_{11}^{22}+a_{22}^{22})\partial_{22}\varphi$$
$$+(b_{11}^1+b_{22}^1)\partial_1\varphi+(b_{11}^2+b_{22}^2)\partial_2\varphi+|\varphi|^2\varphi], \tag{A12}$$

for φ, where ∂_i denotes derivative with respect to ξ_i. Since the mesh is fixed during this phase, x_1 and x_2 remain constant, as do the coefficients a_{ij}^{kl} and b_{ij}^k. Now we calculate X_1 and X_2 from (A6)–(A8) and compare their vector norm with some fixed tolerance $M>0$. If $|(X_1,X_2)|_{L^\infty}>M$ we perform a mesh refinement step, while if $|(X_1,X_2)|_{L^\infty}<M$ we perform an evolution step. We then compute X_1 and X_2 again and repeat the procedure. Since each mesh refinement step tends to decrease $|(X_1,X_2)|_{L^\infty}$ and each evolution step tends to increase it, we soon reach an equilibrium state in which $|(X_1,X_2)|_{L^\infty}$ hovers very close to M and mesh refinement and evolution steps alternate rapidly with one another.

In all cases, we discretized the spatial differential operators using a seven-point scheme in each direction, while the temporal discretization was performed using a variable time step fifth-order Runge-Kutta-Fehlberg scheme with an embedded fourth-order error estimate.

We use parameters $L=6$, $n_1=n_2=120$, and tolerance $M=2$. We first define a smoothing operator S. Let $f=f_{ij}$, $-n_1\leq i\leq n_1,-n_2\leq j\leq n_2$ be any function defined on the logical mesh, and $S(f)$ defined by

$$(S(f))_{i,j}=\sum_{|k|\leq s_1,|l|\leq s_2}c_k d_l f_{i+k,j+l}, \tag{A13}$$

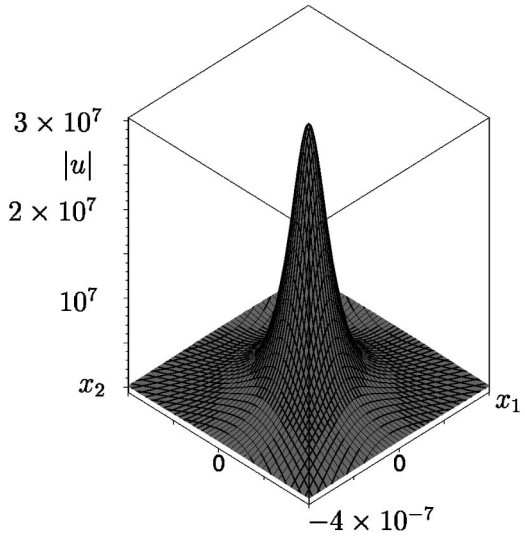

FIG. 16. Single-point blow-up solution of NLS equation: surface plot of u.

where s_1 and s_2 are non-negative integers and c_k and d_l are weights given by a binomial distribution,

$$c_k=\frac{1}{2^{2s_1}}\frac{(2s_1)!}{(s_1-k)!(s_1+k)!},\quad d_l=\frac{1}{2^{2s_2}}\frac{(2s_2)!}{(s_2-l)!(s_2+l)!}. \tag{A14}$$

The formula in Eq. (A13) is valid for $-n_1+s_1\leqslant i\leqslant n_1-s_1$, $-n_2+s_2\leqslant j\leqslant n_2-s_2$. For points near the boundary, it is modified by extrapolating f to fictitious points outside the integration region. The parameters s_1 and s_2 control the degree of smoothing; for $s_1=s_2=0$ the operator S is simply the identity. In effect, S performs a convolution of f with a discrete approximation of a Gaussian centered at the origin. We used this smoothing operator in all of our simulations, and found that it greatly increased the smoothness of the mesh near the singularities, which resulted in improved stability and accuracy.

We now consider the problem of choosing an appropriate weight function. We will consider weight functions that depend only on the value of u and its first- and second-order partial derivatives. Notice that these derivatives are computed relative to the physical variable $\mathbf{x}$ and not the logical variable ξ. In order that the volume under the surface of the function be equidistributed with respect to the new coordinate system, it is desirable to have a mesh spacing that is roughly proportional to the value of $|u|^{-1}$. For example, one can choose $w(u)=(1+|u|^2)^{1/2}$. To extend this result to weight functionals that include higher-order derivative terms, we note that for a self-similar blow-up solution $|u(t)|_{L^\infty}\sim L^{-1}(t)$, $|\partial_i u(t)|_{L^\infty}\sim L^{-2}(t)$, $|\partial_{ij}u(t)|_{L^\infty}\sim L^{-3}(t)$. In order to have a weight function in which all terms remain of equal order as $L(t)\to 0$, we define w as $(c_1,c_2\geqslant 0)$

$$w(u)=S[(1+|u|^6+c_1|\partial_i u|^3+c_2|\partial_{ij}u|^2)^{1/6}], \tag{A15}$$

This is the form of w that will be used for all of our simulations. In the case of single-point blow-up for the scalar NLS equation, the solution u has a relatively simple structure, so for this simulation we took $c_1=c_2=0$ with smoothing parameters $s_1=s_2=6$.

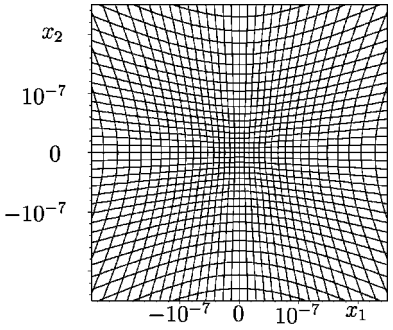

FIG. 17. Closeup view of mesh near the blow-up point.

We were able to perform the integration up to $\tau=177.3$, where we recall that the rescaled time τ is defined by $\tau=\int_0^t|u(s)|_{L^\infty}^2 ds$. This corresponds to a physical time $t=0.145\,443$. At the end of the simulation, the amplitude was approximately 3.0×10^7 and the time step dt was approximately 7.0×10^{-17}. The mesh spacing at the origin was about 10^{-8}, an increase in resolution of about 5×10^6 over the initial grid.

In Fig. 16 we show surface plots of the solution in physical coordinates, while in Fig. 17 we show plots of a blow-up view near the origin.

APPENDIX B: COEFFICIENTS FOR PARTIAL DERIVATIVES IN CURVILINEAR COORDINATES

The coefficients a_{ij}^{kl} and b_{ij}^{k} associated with the formula

$$\frac{\partial^2 u}{\partial x_i\partial x_j}=a_{ij}^{kl}\frac{\partial^2\varphi}{\partial\xi_k\partial\xi_l}+b_{ij}^{k}\frac{\partial\varphi}{\partial\xi_k}, \tag{B1}$$

where $x_1=x_1(\xi_1,\xi_2)$, and $x_2=x_2(\xi_1,\xi_2)$, are curvilinear coordinates given by

$$a_{11}^{11}=\frac{1}{J^2}\left(\frac{\partial x_2}{\partial\xi_2}\right)^2,\quad a_{11}^{12}=-\frac{1}{J^2}\left(\frac{\partial x_2}{\partial\xi_1}\frac{\partial x_2}{\partial\xi_2}\right),$$

$$a_{11}^{22}=\frac{1}{J^2}\left(\frac{\partial x_2}{\partial\xi_1}\right)^2,\quad a_{12}^{22}=-\frac{1}{J^2}\left(\frac{\partial x_1}{\partial\xi_1}\frac{\partial x_2}{\partial\xi_1}\right), \tag{B2}$$

$$b_{11}^{1}=\frac{1}{J}\left[\frac{\partial x_2}{\partial\xi_2}\frac{\partial}{\partial\xi_1}\left(\frac{1}{J}\frac{\partial x_2}{\partial\xi_2}\right)-\frac{\partial x_2}{\partial\xi_1}\frac{\partial}{\partial\xi_2}\left(\frac{1}{J}\frac{\partial x_2}{\partial\xi_2}\right)\right], \tag{B3}$$

$$b_{11}^{2}=\frac{1}{J}\left[\frac{\partial x_2}{\partial\xi_1}\frac{\partial}{\partial\xi_2}\left(\frac{1}{J}\frac{\partial x_2}{\partial\xi_1}\right)-\frac{\partial x_2}{\partial\xi_2}\frac{\partial}{\partial\xi_1}\left(\frac{1}{J}\frac{\partial x_2}{\partial\xi_1}\right)\right], \tag{B4}$$

$$a_{12}^{11}=-\frac{1}{J^2}\left(\frac{\partial x_1}{\partial\xi_2}\frac{\partial x_2}{\partial\xi_2}\right),\quad a_{12}^{12}=\frac{1}{J^2}\left(\frac{\partial x_1}{\partial\xi_1}\frac{\partial x_2}{\partial\xi_2}+\frac{\partial x_1}{\partial\xi_2}\frac{\partial x_2}{\partial\xi_1}\right), \tag{B5}$$

$$b_{12}^{1}=\frac{1}{2J}\left[\frac{\partial x_2}{\partial \xi_1}\frac{\partial}{\partial \xi_2}\left(\frac{1}{J}\frac{\partial x_1}{\partial \xi_2}\right)-\frac{\partial x_2}{\partial \xi_2}\frac{\partial}{\partial \xi_1}\left(\frac{1}{J}\frac{\partial x_1}{\partial \xi_2}\right)\right]+\frac{1}{2J}\left[\frac{\partial x_1}{\partial \xi_1}\frac{\partial}{\partial \xi_2}\left(\frac{1}{J}\frac{\partial x_2}{\partial \xi_2}\right)-\frac{\partial x_1}{\partial \xi_2}\frac{\partial}{\partial \xi_1}\left(\frac{1}{J}\frac{\partial x_2}{\partial \xi_2}\right)\right], \tag{B6}$$

$$b_{12}^{2}=\frac{1}{2J}\left[\frac{\partial x_2}{\partial \xi_2}\frac{\partial}{\partial \xi_1}\left(\frac{1}{J}\frac{\partial x_1}{\partial \xi_1}\right)-\frac{\partial x_2}{\partial \xi_1}\frac{\partial}{\partial \xi_2}\left(\frac{1}{J}\frac{\partial x_1}{\partial \xi_1}\right)\right]+\frac{1}{2J}\left[\frac{\partial x_1}{\partial \xi_2}\frac{\partial}{\partial \xi_1}\left(\frac{1}{J}\frac{\partial x_2}{\partial \xi_1}\right)-\frac{\partial x_1}{\partial \xi_1}\frac{\partial}{\partial \xi_2}\left(\frac{1}{J}\frac{\partial x_2}{\partial \xi_1}\right)\right], \tag{B7}$$

$$a_{22}^{11}=\frac{1}{J^2}\left(\frac{\partial x_1}{\partial \xi_2}\right)^2,\quad a_{22}^{12}=-\frac{1}{J^2}\left(\frac{\partial x_1}{\partial \xi_1}\frac{\partial x_1}{\partial \xi_2}\right),\quad a_{22}^{22}=\frac{1}{J^2}\left(\frac{\partial x_1}{\partial \xi_1}\right)^2, \tag{B8}$$

$$b_{22}^{1}=\frac{1}{J}\left[\frac{\partial x_1}{\partial \xi_2}\frac{\partial}{\partial \xi_1}\left(\frac{1}{J}\frac{\partial x_1}{\partial \xi_2}\right)-\frac{\partial x_1}{\partial \xi_1}\frac{\partial}{\partial \xi_2}\left(\frac{1}{J}\frac{\partial x_1}{\partial \xi_2}\right)\right], \tag{B9}$$

$$b_{22}^{2}=\frac{1}{J}\left[\frac{\partial x_1}{\partial \xi_1}\frac{\partial}{\partial \xi_2}\left(\frac{1}{J}\frac{\partial x_1}{\partial \xi_1}\right)-\frac{\partial x_1}{\partial \xi_2}\frac{\partial}{\partial \xi_1}\left(\frac{1}{J}\frac{\partial x_1}{\partial \xi_1}\right)\right]. \tag{B10}$$

[1] V. Zakharov, Sov. Phys. JETP **35**, 908 (1972).
[2] S. Thornhill and D. ter Haar, Phys. Rep. **43**, 43 (1978).
[3] C. Sulem and P.-L. Sulem, in *The Nonlinear Schroedinger Equation: Self-focusing and Wave Collapse*, Springer Series in Applied Mathematical Sciences Vol. 139 (Springer, Berlin, 1999).
[4] M. Goldman and D. Nicholson, Phys. Rev. Lett. **41**, 406 (1978).
[5] W. Ren and X. Wang, J. Comput. Phys. **159**, 246 (2000).
[6] G. Fibich, W. Ren, and X. Wang (unpublished).
[7] T. Colin and M. Weinstein, Ann. I.H.P. Phys. Theor. **65**, 57 (1996).
[8] J. Coleman, Ph.D. thesis, University of Toronto, Toronto, 2001.
[9] W. Strauss, Commun. Math. Phys. **55**, 149 (1977).
[10] C. Budd, S. Chen, and R. Russell, J. Comput. Phys. **10**, 756 (1999).
[11] C. Budd, SIAM (Soc. Ind. Appl. Math.) J. Appl. Math. **62**, 801 (2002).
[12] D. McLaughlin, G. Papnicolaou, C. Sulem, and P. Sulem, Phys. Rev. A **34**, 1200 (1986).
[13] G. Papanicolaou, C. Sulem, P. Sulem, and X. Wang, Phys. Fluids B **3**, 969 (1991).
[14] S. Champeaux, T. Passot, and P. Sulem, Phys. Plasmas **5**, 100 (1998).
[15] D. Laveder, T. Passot, and P. Sulem, Physica D **152-153**, 694 (2001).
[16] G. Luther, A. Newell, and J. Moloney, Physica D **74**, 59 (1994).
[17] G. Fibich, V. Malkin, and G. Papnicolaou, Phys. Rev. A **52**, 4218 (1995).
[18] L. Bergé, J. Rasmussen, E. Kuznetsov, E. Shapiro, and S. Turitsyn, J. Opt. Soc. Am. B **13**, 1879 (1996).
[19] K. Germaschewski, R. Grauer, L. Bergé, V. Mezentsev, and J. Rasmussen, Physica D **151**, 175 (2001).
[20] P. Knupp and S. Steinberg, *The Fundamental of Grid Generation* (CRC Press, Boca Raton, 1993).
[21] J. Thompson, Z. Warsi, and C. Mastin, *Numerical Grid Generation. Foundations and Applications* (North-Holland, New York, 1985).
[22] J. Brackbill and J. Saltzman, Appl. Math. Comput. **10**, 865 (1982).
[23] A. Winslow, J. Comput. Phys. **135**, 126 (1997).
[24] D. Catherall, Int. J. Numer. Methods Eng. **32**, 921 (1991).
[25] W. Huang, Y. Ren, and R. Russell, J. Comput. Phys. **113**, 279 (1994).
[26] W. Huang, Y. Ren, and R. Russell, SIAM (Soc. Ind. Appl. Math.) J. Numer. Anal. **31**, 709 (1994).
[27] W. Huang and R. Russell, SIAM (Soc. Ind. Appl. Math.) J. Numer. Anal. **34**, 1106 (1997).